Science Bulletin 64 (2019) 1510–1517

Contents lists available at ScienceDirect

Science Bulletin

journal homepage: www.elsevier.com/locate/scib

Science Bulletin
www.scibull.com

Article

# Constructing highly dispersed 0D $Co_3S_4$ quantum dots/2D g-$C_3N_4$ nanosheets nanocomposites for excellent photocatalytic performance

Hongcen Yang, Jiangmei Yin, Ruya Cao, Pengxiao Sun, Shouwei Zhang, Xijin Xu *

*School of Physics and Technology, University of Jinan, Jinan 250022, China*

ARTICLE INFO

*Article history:*
Received 13 May 2019
Received in revised form 4 July 2019
Accepted 23 July 2019
Available online 5 August 2019

*Keywords:*
$Co_3S_4$
g-$C_3N_4$
Photocatalysis

ABSTRACT

The development of noble-metal-free catalysts with high efficiency photocatalytic properties is critical to the heterogeneous catalysis. Herein, zero-dimensional (0D) metal sulfide quantum dots/two-dimensional (2D) g-$C_3N_4$ nanosheets ($Co_3S_4$/CNNS) nanocomposites are synthesized by a two-step method, including the ways of in-situ deposition and water bath. The highly dispersed $Co_3S_4$ quantum dots (particle size is 2–4 nm) are evenly and tightly fixed on CNNS, which can be used as co-catalyst to effectively replace noble metals to improve the photocatalytic properties of CNNS. $Co_3S_4$/CNNS-900 has the apparent quantum efficiency, which is up to 7.85% at 400 nm. At the same time, the $H_2$ evolution rate of $Co_3S_4$/CNNS-900 is 20,536.4 μmol $g^{-1}$ $h^{-1}$, which is 555 times than CNNS. The excellent photocatalytic performance is due to the highly dispersed $Co_3S_4$ quantum dots on 2D CNNS, which facilitate the formation of more active sites, $Co_3S_4$/CNNS promotes the separation and migration of photogenerated carriers, shortens the migration distance of photogenerated carriers, and eventually leads to an increase of the photocatalytic performance.



## 1. Introduction

In recent years, the photocatalytic $H_2$ evolution has caused the researchers' focus. To get efficient solar energy conversion and excellent photocatalytic $H_2$ evolution, ideal photocatalytic materials are one of the key factors, which should have a proper band gap capable of absorbing visible light, can effectively promote separation and migration of photogenerated carriers, and have high stability [1,2]. In addition, the photocatalytic materials should be cheap, nontoxic and easy to process. Among them, g-$C_3N_4$ has induced the research focus for the sufficient redox ability to achieve the decomposition of water and has relatively high $H_2$ evolution performance [3,4]. To enhance the $H_2$ evolution of g-$C_3N_4$-based photocatalytic materials, introducing cocatalyst can promote the separation and migration of photogenerated carriers [5,6]. Noble metals including Pt and Ru are efficient cocatalysts, but are restricted by the high cost [7,8]. Therefore, the development of high-efficiency cocatalysts, which are inexpensive and easy to synthesize, is of great significance for achieving efficient, large-scale photocatalytic $H_2$ evolution [8–10]. Among them, metal sulfides ($Co_3S_4$) as promising cocatalysts have attracted more and more attention, however, they tend to form large particles during the synthesis and have poor dispersibility [11–13]. These properties inevitably lead to the decrease of surface active sites. Therefore, it is still a huge challenge to control the morphology of metal sulfide ($Co_3S_4$) to increase the active sites of photocatalysts for the improvement of the photocatalytic performance [14].

Recently, the research of zero-/two-dimensional (0D/2D) photo/electrocatalysts has been significantly developed, and the stripped 2D g-$C_3N_4$ nanosheets are considered to be one of the most effective methods to provide more reaction sites [14,15]. Furthermore, the unique 2D nanosheets provide a large surface that facilitates the dispersion of nanoparticles [16,17]. For example, Li and co-workers [14] realized $Co_3O_4$ quantum dots modified g-$C_3N_4$ had excellent photocatalytic degradation ability for tetracycline. Xu and co-workers [16] successfully implemented the modifications of g-$C_3N_4$ nanosheets via $MP_x$ nanoparticles, which can greatly enhance the performance of photocatalysts. In addition, Shi et al. [8] synthesized the monodisperse Pt/g-$C_3N_4$ nanocomposites, which exhibit excellent photocatalytic performance. Based on the above design concept, an effective method for increasing photocatalytic $H_2$ evolution performance is to adjust the structural morphologies of catalysts and reduce the size of the nanoparticles, which is advantageous for the formation of more active sites and for the migration of carriers [14,18–20]. At present, Yu and co-workers [12] prepared hollow $CoS_x$/g-$C_3N_4$ nanocomposites

* Corresponding author.
*E-mail address:* sps_xuxj@ujn.edu.cn (X. Xu).

https://doi.org/10.1016/j.scib.2019.08.001

via hydrothermal method for photocatalytic $H_2$ evolution. Li et al. [13] achieved $CoS_2$/g-$C_3N_4$ nanocomposites by simple hydrothermal method and used them to produce hydrogen from photolysis water. Although some exciting results have been achieved, however, the agglomerated or large-sized cobalt sulfide nanoparticles significantly increase the migration distance of photogenerated carriers and reduce the reactive sites [20–24]. Furthermore, the irregular morphologies and random dispersion characteristics of cobalt sulfide result in the inability to fully utilize the 2D nanosheets of g-$C_3N_4$ [25,26]. However, uniform 0D quantum dots have extremely small dimensions (<5 nm) and efficient photocarrier transport efficiency, besides, the tight interaction between 0D and 2D can improve the dispersion and stability of quantum dots [14,16,27,28]. Therefore, the construction of cobalt sulfide quantum dots and g-$C_3N_4$ nanosheets is beneficial to achieve efficient photocatalytic $H_2$ evolution [14,18].

In this work, high-dispersion transition metal sulfide ($Co_3S_4$) quantum dots instead of noble-metal cocatalysts are designed and synthesized to anchor on ultra-thin g-$C_3N_4$ nanosheets by in-situ deposition and water bath methods. The obtained $Co_3S_4$/g-$C_3N_4$ nanosheets (CNNS) nanocomposites exhibit higher photocatalytic $H_2$ evolution than pure CNNS. The rate of $H_2$ evolution is up to 20,536.4 μmol $g^{-1}$ $h^{-1}$ ($Co_3S_4$/CNNS-900). This rate is about 555 times of pure CNNS and 1,579 times of pure $Co_3S_4$, respectively. Our research can provide new ideas for the rational development of efficient, economical and sustainable environmentally friendly nanocomposites.

## 2. Experimental

### 2.1. Synthesis of g-$C_3N_4$ nanosheets (CNNS)

CNNS were prepared by calcining urea. Firstly, urea was placed in the covered crucible and heated under static air at 550 °C for 4 h with a ramp rate of 2.5 °C $min^{-1}$. Then the bulk g-$C_3N_4$ placed in open crucible, and heated at 500 °C for 2 h with a ramp rate of 5 °C $min^{-1}$. After that, CNNS were synthesized [16].

### 2.2. Prepare of $Co(CO_3)_{0.5}(OH)\cdot 0.1H_2O$/CNNS

The $Co(CO_3)_{0.5}(OH)\cdot 0.1H_2O$/CNNS were synthesized through the in-situ precipitation method [16]. Typically, 1 mmol $CoCl_2\cdot 6H_2O$ was dissolved in 150 mL ethanol. Then CNNS (700, 800, 900, 1,000, 1,100 mg) were dispersed into the solution with sonicating for 1 h. After that, 3 mmol $NH_4HCO_3$ was dissolved in the solution and stirred for 6 h. The precipitates were collected and washed with ethanol. After that, $Co(CO_3)_{0.5}(OH)\cdot 0.1H_2O$/CNNS with different amount of CNNS were obtained, recorded as $Co(CO_3)_{0.5}(OH)\cdot 0.1H_2O$, $Co(CO_3)_{0.5}(OH)\cdot 0.1H_2O$/CNNS-700, $Co(CO_3)_{0.5}(OH)\cdot 0.1H_2O$/CNNS-900, $Co(CO_3)_{0.5}(OH)\cdot 0.1H_2O$/CNNS-1100 and CNNS, respectively.

### 2.3. Synthesis of $Co_3S_4$/CNNS

Typically, a certain amount of $Co(CO_3)_{0.5}(OH)\cdot 0.1H_2O$/CNNS nanocomposites was dissolved in 400 mL water. Then, thioacetamide (10× the mass of $Co(CO_3)_{0.5}(OH)\cdot 0.1H_2O$/CNNS nanocomposites) was dispersed into the solution with sonicating for 0.5 h. After that, the solution was heated at 90 °C for 1 h. The precipitates were washed with water. Then, $Co_3S_4$/CNNS nanocomposites with different contents of CNNS were obtained and labeled as $Co_3S_4$, $Co_3S_4$/CNNS-700, $Co_3S_4$/CNNS-900, $Co_3S_4$/CNNS-1100 and CNNS.

### 2.4. Characterizations

A D/MAX2500 V diffractometer was used to measure the powder X-ray diffraction (XRD). The test of UV–vis was investigated by Shimadzu UV-2500 spectrophotometer, which used $BaSO_4$ as reference. Structural information was obtained by Fourier transform spectrophotometer (FT-IR, Avatar 370, Thermo Nicolet). The data of X-ray photoelectron spectroscopy (XPS) were obtained by the instrument of ESCALAB250. Scanning electron microscope (SEM) and transmission electron microscope (TEM) images were achieved via the JEOL JSM-6330F SEM and JEOL-2100 field emission TEM. The photoluminescence spectra (PL) were measured by Shimadzu RF-6000. The type of time-resolved technique is Bruker S8 Tiger. The $H_2$-solar system (Beijing Aulight Co.) with a gas chromatogram (GC) was used to collect and detect $H_2$ online. Transient photocurrent responses and electrochemical impedance spectroscopy were conducted in three-electrode cell system by using a CHI660E electrochemical station, 50 mW LED as light source and 1 mol $L^{-1}$ $Na_2SO_4$ solution as electrolyte.

### 2.5. Photocatalytic tests

The photocatalytic $H_2$ evolution was tested in 500 mL Pyrex glass cell. A 300 W Xe lamp was used as the light source. In general, the reaction solution contains 100 mL water, 20 mg $Co_3S_4$/CNNS photocatalyst and 20 mL triethanolamine (TEOA) which served as sacrificial agents. A controlled experiment was carried out by using P25 as a standard photocatalyst, and the reaction solution contains 100 mL water, 50 mg P25, 300 μL $H_2PtCl_6$ (10 g $L^{-1}$) and 20 mL methanol which served as sacrificial agents. Before irradiation, the reaction system was pumped to vacuum and ensured the reaction system in an anaerobic condition. The level of the vacuum is −0.1 MPa. All glasswares were carefully rinsed with distilled water prior to use. The $H_2$ evolution rates on $Co_3S_4$/CNNS were measured with different irradiation wavelengths with band-pass filters of 365 ± 5, 380 ± 5, 400 ± 5, 420 ± 5, 450 ± 5, 475 ± 5, 500 ± 5, 550 ± 5 and 600 ± 5 nm. The apparent quantum efficiency (AQE) of the catalyst for $H_2$ evolution was measured by applying a Xe lamp (300 W) with a 400 ± 5 nm band-pass filter.

$$\mathrm{AQE}(\%) = \frac{\text{number of reacted electrons}}{\text{number of incident photons}} \times 100 = \frac{\text{number of evolved } H_2 \text{ molecules} \times 2}{\text{number of incident photons}} \times 100. \quad (1)$$

## 3. Results and discussion

In order to determine the metal species of the material obtained in the first step, XRD was measured (Fig. S1 online). It can be observed that the metal products of Co belong to basic carbonates ($Co(CO_3)0.5(OH)\cdot 0.1H_2O$). After comparison with the PDF cards of XRD, the metal species of Co correspond to PDF No. 48-0038, which represents $Co(CO_3)0.5(OH)\cdot 0.1H_2O$. Therefore, $Co(CO_3)0.5(OH)\cdot 0.1H_2O$/CNNS nanocomposites were obtained in the first step. The XRD of CNNS, $Co_3S_4$ and $Co_3S_4$/CNNS-900 are displayed in Fig. 1a. Two characteristic diffraction peaks of CNNS at 12.9° and 27.5° are clearly identified as (1 0 0) and (0 0 2) diffraction plane (JCPDS No. 87-1526) [26,29]. The peaks at 31.1°, 36.2°, 47.1° and 55.3° are attributed to the $Co_3S_4$ (JCPDS No. 42-1448), which are (3 1 1), (4 0 0), (4 2 2) and (4 4 0), respectively [11,18,25,30]. No diffraction peaks of $Co_3S_4$ among $Co_3S_4$/CNNS nanocomposites can be observed, which is due to the low load of $Co_3S_4$ quantum dots and the relative low crystallinity [14,16]. These results mean that the loaded $Co_3S_4$ quantum dots do not change the morphologies and structures of CNNS, and the content of $Co_3S_4$ quantum

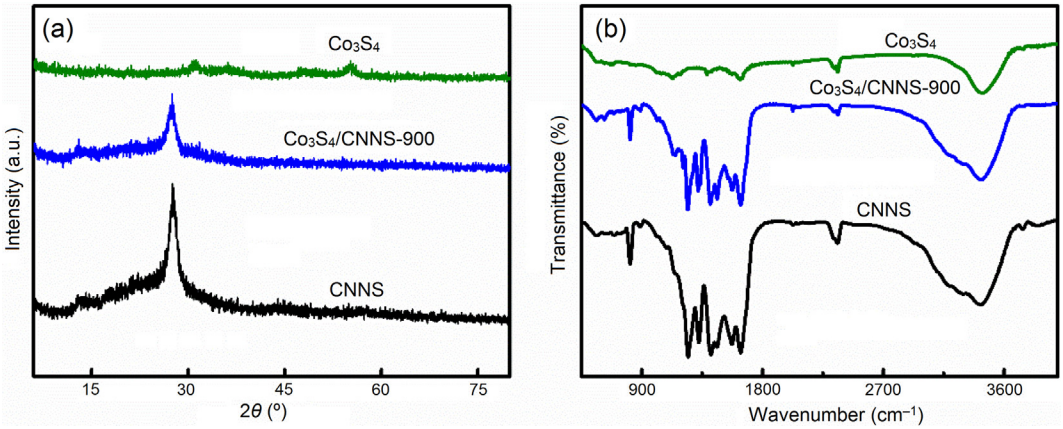


**Fig. 1.** (Color online) XRD patterns (a) and FT-IR spectra (b) of CNNS, $Co_3S_4$ and $Co_3S_4$/CNNS nanocomposites.

dots is low in the composite photocatalysts [16,31]. Fig. 1b shows FT-IR of pure CNNS, pure $Co_3S_4$ and $Co_3S_4$/CNNS. For CNNS and $Co_3S_4$/CNNS, in the range of 780–1,800 $cm^{-1}$, the broad adsorption bands represent s-triazine ring units and heptazine heterocyclic ring units [29,32]. The adsorption bands at 2,950–3,710 $cm^{-1}$ are the O—H bands and residual N—H components, which correspond to uncondensed amino groups and surface-adsorbed $H_2O$ [9,17]. It can be observed that all nanocomposites have a small peak between 2,300 and 3,400 $cm^{-1}$. The small peaks between 2,300 and 2,600 $cm^{-1}$ are attributed to the appearance of C≡N and N═C═N, which might be from the small fragment of diazo groups adhered to the surface. In fact, these might have no impact on the formation of the organic network structure. Moreover, no obvious bands can be found from the FT-IR spectrum of $Co_3S_4$. The results illustrate that $Co_3S_4$/CNNS nanocomposites do not change the structure of CNNS, which is as same as the XRD analysis [14,16].

Thermogravimetric analysis was carried out to determine the content of $Co_3S_4$ in $Co_3S_4$/CNNS-900. As shown in Fig. S2 (online), the weight of $Co_3S_4$/CNNS-900 reduces rapidly, which occurs from about 200 to 650 °C due to the burning of $Co_3S_4$ and CNNS. When the temperature reached 800 °C, CNNS are completely burned out, and the residue is $Co_3O_4$. So the contents of $Co_3S_4$ can be calculated by the content of $Co_3O_4$ using the Eqs. (2), (3).

$$M_{\text{metaloxide}} = \frac{m \times \text{weight loss rate}}{M_{\text{r-metaloxide}}}, \tag{2}$$

where, $M$: molar mass, $M_r$: the relative molecular mass, $m$: total mass of the composite. In addition, the molar mass of $Co_3O_4$ is consistent with the molar mass of $Co_3S_4$. So the content of $Co_3S_4$ could be obtained by

$$\text{Content of } Co_3S_4 = \frac{M \times M_r}{m} \times 100\%. \tag{3}$$

The content of $Co_3O_4$ can be obtained from the weight loss of the composites, which is 12.87% ($Co_3O_4$). The total mass of $Co_3S_4$/CNNS-900 is 7.155 g, herein, the content of $Co_3S_4$ in $Co_3S_4$/CNNS-900 is calculated to be 16.3%.

As shown in Fig. 2a, UV–vis diffuse reflection spectra indicate that the absorption band edge of CNNS is about 435 nm (bang gap is ~2.85 eV). The band gap energy ($E_g$) of CNNS and $Co_3S_4$ can be calculated by $\alpha h\nu = A(h\nu - E_g)^{n/2}$ ($n = 1$ for direct transition and $n = 4$ for indirect transition) [22]. So the bang gap of CNNS is ~2.85 eV, and the bang gap of $Co_3S_4$ quantum dot is 1.6 eV (as shown in Fig. 2b) [22]. In addition, from the Mott-Schottky plots of $Co_3S_4$ and CNNS (Fig. S3 online), it can be known that the conduction bands (CB) of $Co_3S_4$ and CNNS are −0.90 and −1.41 eV, respectively. So the valence bands (VB) of $Co_3S_4$ and CNNS are 0.70 and 1.44 eV respectively. Observed from Fig. 2a, the absorption edges of $Co_3S_4$/CNNS slightly shift to the longer wavelength in comparison with CNNS. This is ascribed to the optical absorption of $Co_3S_4$ quantum dots [21,23]. The red shift means that $Co_3S_4$/CNNS nanocomposites can absorb more visible light and will

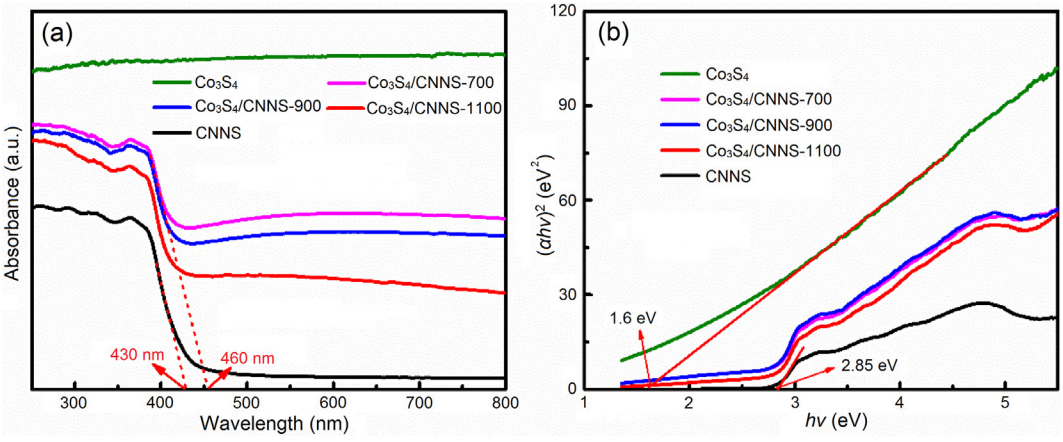


**Fig. 2.** (Color online) Light absorption characteristics and band gaps of photocatalysts. (a) UV–vis diffuse reflectance spectra of CNNS, $Co_3S_4$ and $Co_3S_4$/CNNS nanocomposites. (b) Plot of $(\alpha h\nu)^2$ vs. $h\nu$ for the band gap energies of CNNS, $Co_3S_4$ and $Co_3S_4$/CNNS nanocomposites.

generate more electron-hole pairs [33,34]. In addition, the $Co_3S_4$/CNNS nanocomposite in the visible region has higher light absorption intensity than pure CNNS. All of these are beneficial to improve the photocatalytic performance.

The morphologies and structures of CNNS, $Co_3S_4$ and $Co_3S_4$/CNNS nanocomposites are shown in Fig. 3. As shown in Fig. 3a, d, CNNS are composed of ultra-thin nanosheets with pleats. Fig. 3b, e indicates that pure $Co_3S_4$ is composed of some irregular particles, and the lattice spacing is 0.28 nm, demonstrating the synthesis of $Co_3S_4$ [25]. Fig. 3c, f presents the TEM images of $Co_3S_4$/CNNS-900. It can be observed that the sizes of $Co_3S_4$ quantum dots are 2–4 nm, and the morphology of the nanocomposites does not change significantly compared with pure CNNS. The elemental mapping of $Co_3S_4$/CNNS-900 in Fig. 3g demonstrates the existence of highly dispersed Co, S, C, and N elements in the nanocomposites. The characterizations indicate that $Co_3S_4$ exists in the quantum dots and is uniformly dispersed on CNNS. The surface components and chemical states of pure CNNS, $Co_3S_4$ and $Co_3S_4$/CNNS-900 are further studied by XPS. The results are shown in Fig. 4. C and N in CNNS, Co and S in $Co_3S_4$, C, N, Co and S in $Co_3S_4$/CNNS-900 are observed. For C 1s in Fig. 4a, three peaks at 284.8, 286.0 and 288.1 eV are presented. The peak at 284.8 eV belongs to the graphite-like carbon (C—C/C=C), and the peaks at 286.0 and 288.4 eV represent $sp^3$ carbon bond (C—N) and $sp^2$ carbon bond (N—C=N), respectively [5,8,35]. Fig. 4b displays the N 1s spectra of CNNS and $Co_3S_4$/CNNS-900, which can be fitted with four peaks with binding energies of 398.4, 399.6, 400.9, and 404.3 eV [16,32,36]. The peak at 398.4 eV is the N $sp^2$ bond in the triazine C—N=C ring, and the peaks at 399.6 and 400.9 eV correspond to the tertiary nitrogen group (N—$(C)_3$) and the quaternary N three carbon atom amino functional group (N—H) in the aromatic ring, respectively [27,29,31]. In addition, the peak at 404.2 eV is π excitation [37,38]. For $Co_3S_4$ and $Co_3S_4$/CNNS-900, Co 2p can fit six peaks as shown in Fig. 4c. Two peaks at 778.9 and 793.9 eV correspond to Co $2p_{3/2}$ and Co $2p_{1/2}$ in $Co_3S_4$ [28,30,31,39]. The other peaks at 780.8 and 797.0 eV belong to $2p_{3/2}$ and $2p_{1/2}$ of Co in cobalt sulfide formed on the surface of CNNS, respectively [25,30]. The peaks at 785.1 and 802.3 eV are two vibrating satellite peaks [39,40]. The S 2p spectra of $Co_3S_4$ and $Co_3S_4$/CNNS-900 are fitted to four peaks with binding energies of 161.8, 163.1, 165.1 and 168.7 eV (Fig. 4d) [18,40]. The fitted peaks at 161.8 and 163.1 eV belong to S $2p_{3/2}$ and S $2p_{1/2}$ in $Co_3S_4$, and the peaks at 165.1 and 168.7 eV belong to S in $SO_3^{2-}$ and $SO_4^{2-}$, respectively [11,12,41]. These results demonstrate the formation of $Co_3S_4$ quantum dots, which is successfully loaded on CNNS.

The $H_2$ productions of pure CNNS, $Co_3S_4$ and $Co_3S_4$/CNNS in Fig. 5a present a linear relationship with time, meaning the stability of the photocatalyst under visible light. In addition, in Fig. 5b, pure CNNS have a relatively low photocatalytic activity (37.22 μmol $g^{-1}$ $h^{-1}$). This is due to the low absorption of visible light and the rapid recombination of carriers. Pure $Co_3S_4$ nanoparticles also have a very small and negligible photocatalytic effect (12.75 μmol $g^{-1}$ $h^{-1}$, Fig. 5b). After loading $Co_3S_4$ quantum dots onto CNNS, the photocatalytic activities of $Co_3S_4$/CNNS

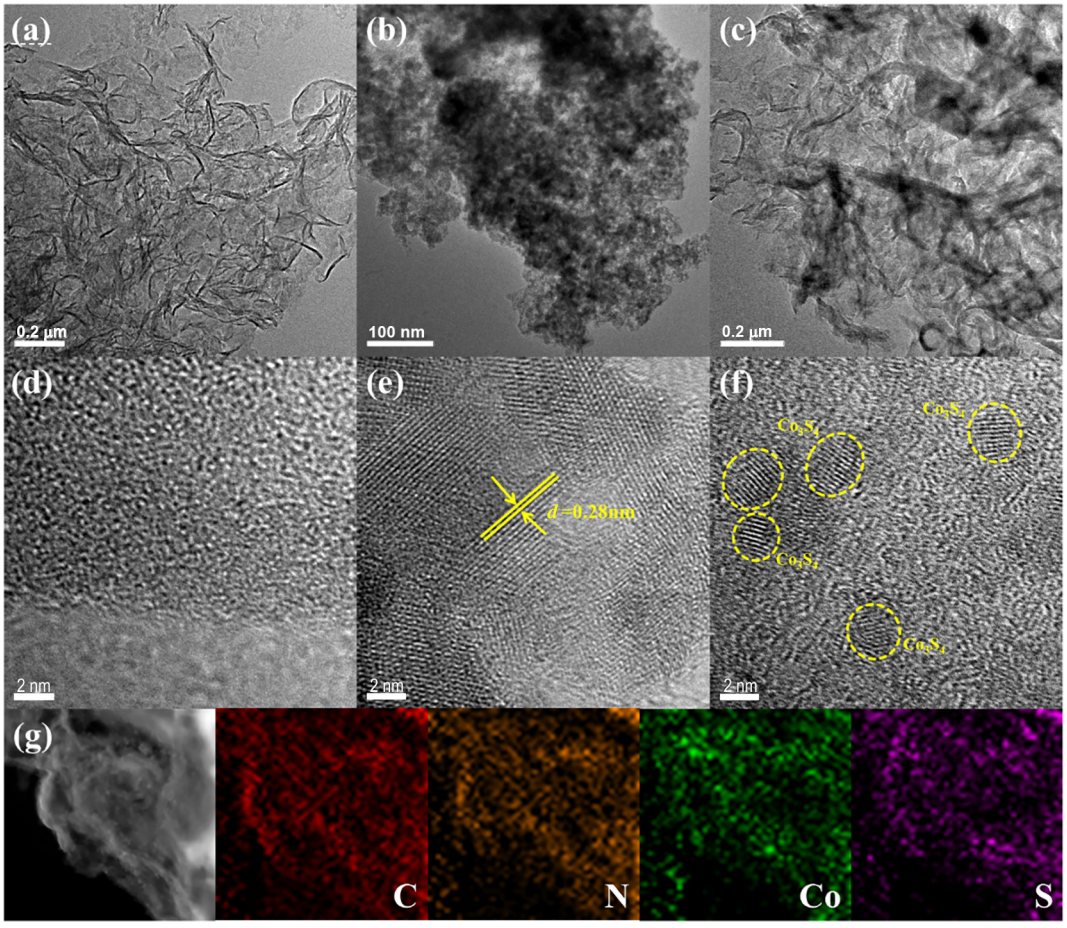


**Fig. 3.** (Color online) Morphological and structural characterizations of photocatalysts. TEM images of CNNS (a, d), $Co_3S_4$ (b, e), $Co_3S_4$/CNNS-900 (c, f) and the elemental mapping of $Co_3S_4$/CNNS-900 (g).

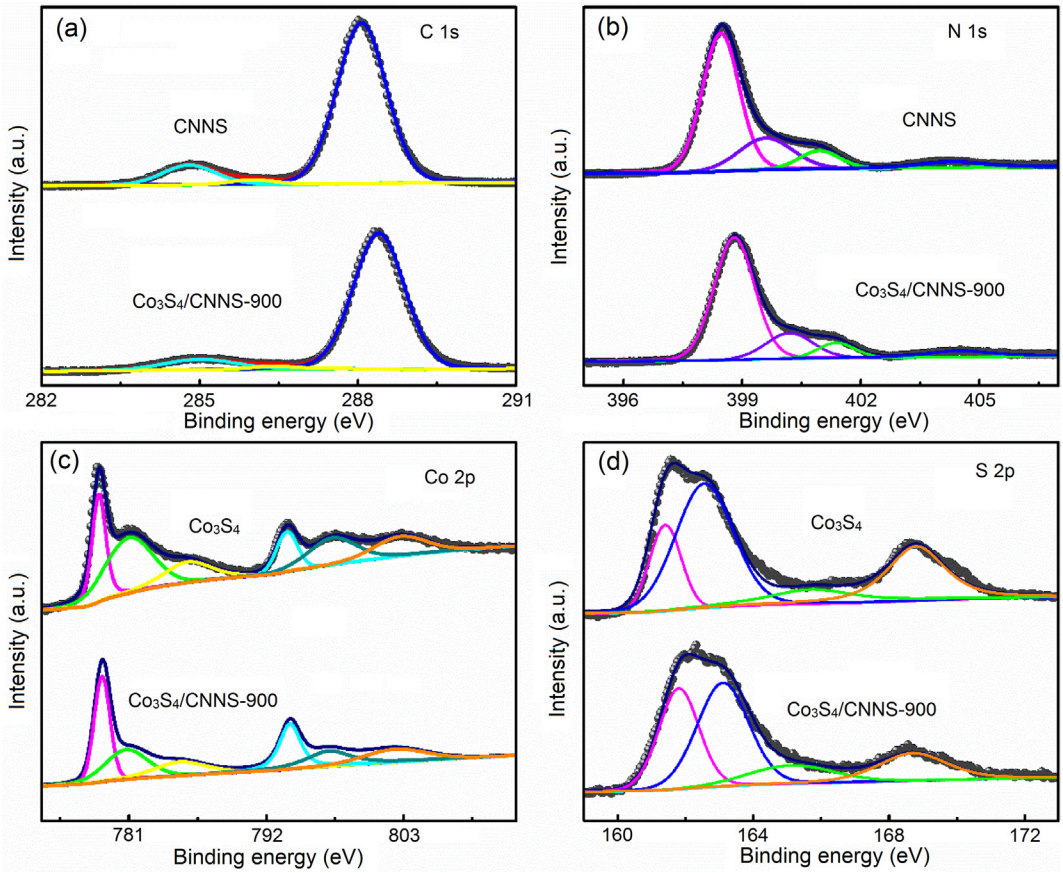


**Fig. 4.** (Color online) High resolution spectra of C 1s (a) and N 1s (b) for CNNS and $Co_3S_4$/CNNS-900. High resolution spectra of Co 2p (c) and S 2p (d) for $Co_3S_4$ and $Co_3S_4$/CNNS-900.

nanocomposites are significantly improved. By regulating the contents of CNNS in the $Co_3S_4$/CNNS nanocomposites, the optimum $H_2$ evolution rate is 20,536 μmol $g^{-1}$ $h^{-1}$, which belongs to $Co_3S_4$/CNNS-900. The $H_2$ evolution rates of $Co_3S_4$/CNNS-700 and $Co_3S_4$/CNNS-1100 (Fig. 5b) are 13,196.6 and 10,700.3 μmol $g^{-1}$ $h^{-1}$, respectively. These are higher than that of pure CNNS and $Co_3S_4$ nanoparticles. The photocatalytic $H_2$ evolution performance of $Co_3S_4$/CNNS-700 is lower than that of $Co_3S_4$/CNNS-900, which is due to the shielding effect of the excessively loaded $Co_3S_4$ quantum dots on the $Co_3S_4$/CNNS-700. In addition, Fig. S4 (online) shows the typical $H_2$-evolution kinetics of S/CNNS under visible light irradiation. Within 4 h of visible-light irradiation, the amount of photocatalytic $H_2$ production of S/CNNS is 281.06 μmol $g^{-1}$. Compared with CNNS, there is no significant change in the photocatalytic performance of CNNS after vulcanization by water bath (90 °C). This means that the effect of vulcanization on CNNS is ruled out during vulcanization. Fig. S5 (online) shows the typical $H_2$-evolution kinetics of Pt/CNNS under visible light irradiation. Under the same conditions of the loading of Pt and $Co_3S_4$, the amount of photocatalytic $H_2$ production of Pt/CNNS is 138,499.6 μmol $g^{-1}$. The average rates of photocatalytic $H_2$ production over Pt/CNNS is 34,624.9 μmol $g^{-1}$ $h^{-1}$. The excellent photocatalytic $H_2$ evolution performance of $Co_3S_4$/CNNS-900 indicates that $Co_3S_4$ quantum dots as cocatalysts are a good substitute for noble metals, which is beneficial to the large-scale application of photocatalysts. In addition, the $H_2$ productions of P25 in Fig. S6 (online) present a linear relationship with time, and the $H_2$ evolution rate of P25 is 26,602.5 μmol $g^{-1}$ $h^{-1}$, which is higher than that of $Co_3S_4$/CNNS-900. After six cycles, the $H_2$ production of $Co_3S_4$/CNNS-900 reduces only ~6% from 82,145.7 to 77,145.6 μmol $g^{-1}$ as shown in Fig. 5c. The results indicate that $Co_3S_4$ quantum dots can be used as cocatalysts to effectively enhance photocatalytic performance of CNNS. Fig. 5d shows the dependence of the quantum efficiency of photocatalytic $H_2$ evolution on $Co_3S_4$/CNNS-900. It can be found that the light with different wavelengths has significant effect on the $H_2$ evolution efficiency of the photocatalysts, and the quantum efficiency of $Co_3S_4$/CNNS-900 at 400 nm is as high as 7.85%. These results demonstrate that the introduction of $Co_3S_4$ quantum dots significantly improves the light absorption properties of CNNS and broadens its photoresponse intensity in the visible region.

To explain the separation, migration and recombination of photogenerated carriers in nanomaterials, photoluminescence spectra (PL), time-resolved spectrum, transient photocurrent response and electrochemical impedance spectroscopy analysis (EIS) are studied [42,43]. PL of pure CNNS, $Co_3S_4$ and $Co_3S_4$/CNNS in Fig. 6a present that the emission peak is ~430 nm, and the excitation light is 325 nm [16]. It can be observed that the peak intensity of $Co_3S_4$/CNNS is much lower than CNNS, with the order of $Co_3S_4$ < $Co_3S_4$/CNNS-900 < $Co_3S_4$/CNNS-700 < CNNS, which is related to the photocatalytic $H_2$ production. The quenching of the CNNS PL suggests that charge transferred to $Co_3S_4$ before recombination takes place, and more photogenerated electrons migrate to the surface of photocatalysts, ultimately improving the performance of photocatalytic $H_2$ production. To get the lifetime of photogenerated electrons, the time-resolved photoluminescence measurements were performed on CNNS, $Co_3S_4$/CNNS-900 and $Co_3S_4$, as displayed in Fig. 6b. The data of time-resolved fluorescence was shown in Table S1 (online). The average radiative lifetime ($t$) was calculated according to the following

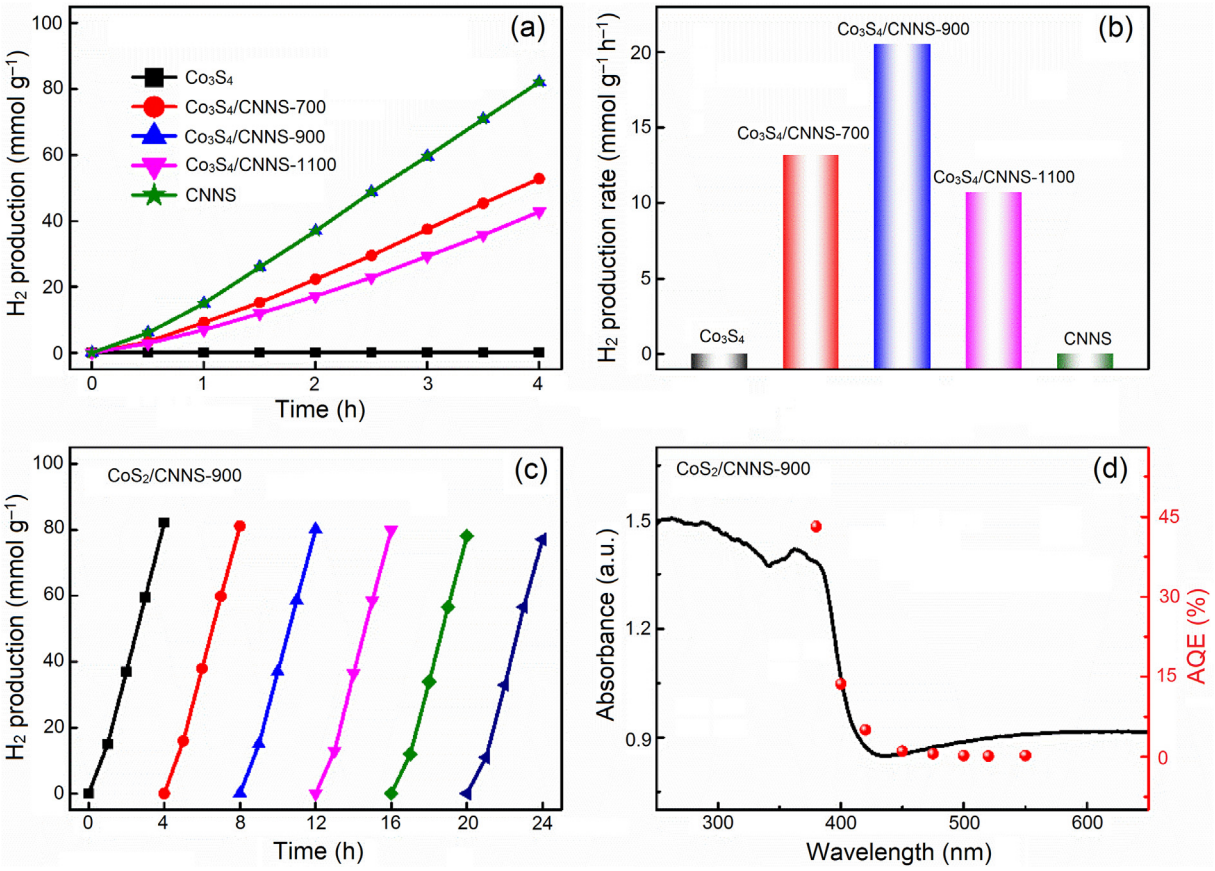


**Fig. 5.** (Color online) Photocatalytic tests of CNNS, $Co_3S_4$, and $Co_3S_4$/CNNS nanocomposites. Time courses (a) and the average rate of $H_2$ evolution (b) over CNNS, $Co_3S_4$, and $Co_3S_4$/CNNS nanocomposites. (c) Cycling test of photocatalytic $H_2$ generation of $Co_3S_4$/CNNS-900. (d) Wavelength dependence of AQE of $Co_3S_4$/CNNS-900 for the $H_2$ evolution (right axis) and UV–vis absorption spectrum of $Co_3S_4$/CNNS-900 (left axis).

$$t = \frac{A_1 \times t_1 \times t_1 + A_2 \times t_2 \times t_2}{A_1 \times t_1 + A_2 \times t_2}. \quad (4)$$

So the average radiative lifetimes of $Co_3S_4$, $Co_3S_4$/CNNS-900 and CNNS are 0.34, 2.54 and 1.49 ns, respectively. The time-resolved spectra demonstrate that the average lifetime of photogenerated electrons in $Co_3S_4$/CNNS-900 is longer than those of CNNS and $Co_3S_4$ quantum dots [44]. The results indicate that the transfer of photogenerated carriers between CNNS and $Co_3S_4$ can extend the lifetime of photogenerated carriers, increase the number of photo-generated electrons, and improve the performance of photocatalytic $H_2$ evolution. The extension of time means that the possibility of photogenerated electrons or holes participating in the photocatalytic reaction is increased [45]. Combined with PL measurement, it can be concluded that the modification of $Co_3S_4$ quantum dots can effectively inhibit the recombination of photo-generated carriers of CNNS, and greatly increase the light conversion efficiency of visible light [46–48]. Transient photocurrent responses in Fig. 6c exhibit a relatively stable photocurrent response over several switching cycles for the samples. Compare with pure CNNS and $Co_3S_4$, $Co_3S_4$/CNNS-700 and $Co_3S_4$/CNNS-900 have higher photocurrent intensity with the order of $Co_3S_4$/CNNS-900 > $Co_3S_4$/CNNS-700 > CNNS > $Co_3S_4$. $Co_3S_4$/CNNS-700 exhibits second-order photocurrent intensity, which is the same as the $H_2$ production effect of $Co_3S_4$/CNNS nanocomposites. These results indicate the improvement of photo-generated carriers' separation and migration efficiency in nanocomposites, and further promote photocatalytic $H_2$ evolution performance [19]. The migration rates of photogenerated carriers are further studied by EIS. As shown in Fig. 6d, pure CNNS have large arc radius, and pure $Co_3S_4$ has the smallest arc radius, which is due to the polymer properties of CNNS and the good conductivity of $Co_3S_4$. And the arc radius of $Co_3S_4$/CNNS-700 and $Co_3S_4$/CNNS-900 are significantly lower than CNNS, in order of $Co_3S_4$ < $Co_3S_4$/CNNS-900 < $Co_3S_4$/CNNS-700 < CNNS. This is consistent with the $H_2$ evolution effect of $Co_3S_4$/CNNS nanocomposites, which means that the transfer resistance of the interface electrons in the $Co_3S_4$/CNNS nanocomposites is much smaller than that of the CNNS [46,48,49]. Furthermore, it also means that $Co_3S_4$/CNNS nanocomposites have higher photo-generated carriers' separation and transfer efficiency. According to the above analysis, the load of $Co_3S_4$ quantum dots can effectively improve the separation and migration rate of the photogenerated carriers of CNNS, and the photocatalytic $H_2$ evolution performance.

Based on the discussions, the reaction mechanism of photocatalytic reaction of $Co_3S_4$/CNNS is proposed (Scheme 1). Under visible light, electrons in valence band of CNNS migrate to conduction band and form holes on valence band, while holes on valence band are consumed by triethanolamine. The electrons are then further transferred to the $Co_3S_4$ quantum dots. In the process, $Co_3S_4$ quantum dots are storage sites of electrons and inhibit the recombination of photogenerated electron-hole pairs, and achieve a large number of active sites for photocatalytic $H_2$ evolution. Thereafter, the electrons that have migrated from the CNNS to the $Co_3S_4$ quantum dots further react with the $H_2O$ molecules to form $H_2$, which are captured on the surface of the photocatalysts.

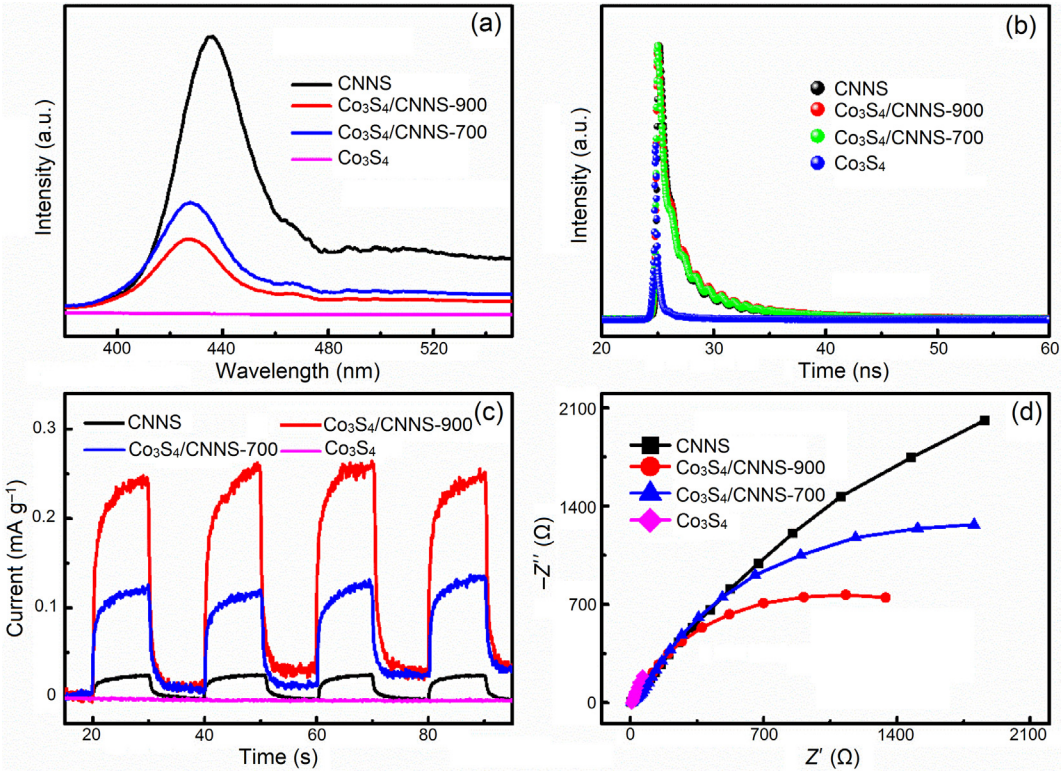


**Fig. 6.** (Color online) Photocatalytic mechanism of CNNS, $Co_3S_4$ and $Co_3S_4$/CNNS nanocomposites. (a) Photoluminescence spectra, (b) time-resolved spectra, (c) transient photocurrent responses, and (d) electrochemical impedance spectroscopies of CNNS, $Co_3S_4$ and $Co_3S_4$/CNNS nanocomposites.

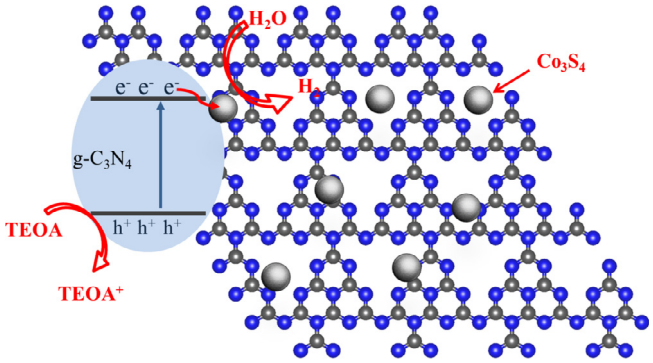


**Scheme 1.** (Color online) Proposed mechanisms of photogenerated charge separation and transfer in the photocatalytic $H_2$ production for the $Co_3S_4$/CNNS nanocomposites.

## 4. Conclusions

In this work, the $Co_3S_4$/CNNS were prepared via two-step process (in-situ deposition and water bathing). The modification of CNNS by highly dispersed $Co_3S_4$ quantum dots realize the high-efficiency photocatalytic $H_2$ evolution performance, in which $Co_3S_4$ quantum dots provide more active sites for photocatalytic $H_2$ evolution, greatly broaden visible light range of CNNS, facilitate the separation and migration of photogenerated carriers and shorten the migration distance of photogenerated electrons. The obtained $Co_3S_4$/CNNS nanocomposites have better photocatalytic performance than pure CNNS, and the highest rate of photocatalytic $H_2$ evolution is 20,536.4 μmol $g^{-1}$ $h^{-1}$ ($Co_3S_4$/CNNS-900), which is about 555 and 1,579 times of pure CNNS and $Co_3S_4$, respectively. This work provides new ideas for the rational development of efficient, economical and sustainable environmentally friendly nanocomposites.

## Conflict of interest

The authors declare that they have no conflict of interest.

## Acknowledgments

This work was supported by the National Natural Science Foundation of China (51672109), and the Natural Science Foundation of Shandong Province for Excellent Young Scholars (ZR2016JL015).

## Author contributions

Xijin Xu designed the experiments and analyzed the data. Shouwei Zhang and Hongcen Yang carried out and analyzed the experimental results. Jiangmei Yin, Ruya Cao and Pengxiao Sun performed the morphological and structural observations.

## Appendix A. Supplementary material

Supplementary material to this article can be found online at https://doi.org/10.1016/j.scib.2019.08.001.

## References

[1] Fu J, Yu J, Jiang C, et al. g-$C_3N_4$-based heterostructured photocatalysts. Adv Energy Mater 2018;8:1701503.
[2] Jing L, Zhu R, Phillips DL, et al. Effective prevention of charge trapping in graphitic carbon nitride with nanosized red phosphorus modification for superior photo(electro)catalysis. Adv Funct Mater 2017;27:1703484.
[3] Li Y, Yang M, Xing Y, et al. Preparation of carbon-rich g-$C_3N_4$ nanosheets with enhanced visible light utilization for efficient photocatalytic hydrogen production. Small 2017;13:1701552.
[4] Liang Q, Li Z, Huang ZH, et al. Holey graphitic carbon nitride nanosheets with carbon vacancies for highly improved photocatalytic hydrogen production. Adv Funct Mater 2015;25:6885–92.

[5] Lu X, Wang Y, Zhang X, et al. NiS and $MoS_2$ nanosheet co-modified graphitic $C_3N_4$ ternary heterostructure for high efficient visible light photodegradation of antibiotic. J Hazard Mater 2018;341:10–9.
[6] Mamba G, Mishra AK. Graphitic carbon nitride (g-$C_3N_4$) nanocomposites: a new and exciting generation of visible light driven photocatalysts for environmental pollution remediation. Appl Catal B Environ 2016;198:347–77.
[7] Ong WJ, Tan LL, Ng YH, et al. Graphitic carbon nitride (g-$C_3N_4$)-based photocatalysts for artificial photosynthesis and environmental remediation: are we a step closer to achieving sustainability? Chem Rev 2016;116:7159–329.
[8] Shi L, Yang L, Zhou W, et al. Photoassisted construction of holey defective g-$C_3N_4$ photocatalysts for efficient visible-light-driven $H_2O_2$ production. Small 2018;14:1703142.
[9] Shi X, Fujitsuka M, Kim S, et al. Faster electron injection and more active sites for efficient photocatalytic $H_2$ evolution in g-$C_3N_4$/$MoS_2$ hybrid. Small 2018;14:1703277.
[10] Sun P, He W, Yang H, et al. Hedgehog-inspired nanostructures for hydrogel-based all-solid-state hybrid supercapacitors with excellent flexibility and electrochemical performance. Nanoscale 2018;10:19004–13.
[11] Chen H, Wang MQ, Yu Y, et al. Assembling hollow cobalt sulfide nanocages array on graphene-like manganese dioxide nanosheets for superior electrochemical capacitors. ACS Appl Mater Interfaces 2017;9:35040–7.
[12] Fu J, Bie C, Cheng B, et al. Hollow $CoS_x$ polyhedrons act as high-efficiency cocatalyst for enhancing the photocatalytic hydrogen generation of g-$C_3N_4$. ACS Sustain Chem Eng 2018;6:2767–79.
[13] Li H, Deng P, Hou Y. Cobalt disulfide/graphitic carbon nitride as an efficient photocatalyst for hydrogen evolution reaction under visible light irradiation. Mater Lett 2018;229:217–20.
[14] Gao H, Yang H, Xu J, et al. Strongly coupled g-$C_3N_4$ nanosheets-$Co_3O_4$ quantum dots as 2D/0D heterostructure composite for peroxymonosulfate activation. Small 2018;14:1801353.
[15] Guo F, Shi W, Zhu C, et al. CoO and g-$C_3N_4$ complement each other for highly efficient overall water splitting under visible light. Appl Catal B Environ 2018;226:412–20.
[16] Yang H, Cao R, Sun P, et al. Highly dispersed and noble metal-free $MP_x$ (M = Ni, Co, Fe) coupled with g.$C_3$N4 nanosheets as 0D/2D photocatalysts for hydrogen evolution. Appl Surface Sci 2018;458:893–902.
[17] Weng CC, Ren JT, Hu ZP, et al. Nitrogen-doped defect-rich graphitic carbon nanorings with $CoO_x$ nanoparticles as highly efficient electrocatalyst for oxygen electrochemistry. ACS Sustain Chem Eng 2018;6:15811–21.
[18] Zhu Y, Xu Y, Hou Y, et al. Cobalt sulfide modified graphitic carbon nitride semiconductor for solar hydrogen production. Int J Hydrog Energy 2014;39:11873–9.
[19] Zhao H, Sun S, Jiang P, et al. Graphitic $C_3N_4$ modified by $Ni_2P$ cocatalyst: an efficient, robust and low cost photocatalyst for visible-light-driven $H_2$ evolution from water. Chem Eng J 2017;315:296–303.
[20] Zhang H, Tian W, Zhou L, et al. Monodisperse $Co_3O_4$ quantum dots on porous carbon nitride nanosheets for enhanced visible-light-driven water oxidation. Appl Catal B Environ 2018;223:2–9.
[21] Zhang S, Gao H, Liu X, et al. Hybrid 0D-2D nanoheterostructures: In situ growth of amorphous silver silicates dots on g-$C_3N_4$ nanosheets for full-spectrum photocatalysis. ACS Appl Mater Interfaces 2016;8:35138–49.
[22] Xu P, Tyler J, Thomas E, et al. Flat-band potentials of molecularly thin metal oxide nanosheets. ACS Appl Mater Interfaces 2016;8:11539–47.
[23] Zhang S, Gao H, Huang Y, et al. Ultrathin g-$C_3N_4$ nanosheets coupled with amorphous Cu-doped FeOOH nanoclusters as 2D/0D heterogeneous catalysts for water remediation. Environ Sci Nano 2018;5:1179–90.
[24] Shao P, Tian J, Liu B, et al. Morphology-tunable ultrafine metal oxide nanostructures uniformly grown on graphene and their applications in the photo-fenton system. Nanoscale 2015;7:14254–63.
[25] Zhang F, Zhuang HQ, Song J, et al. Coupling cobalt sulfide nanosheets with cadmium sulfide nanoparticles for highly efficient visible-light-driven photocatalysis. Appl Catal B Environ 2018;226:103–10.
[26] Zeng D, Ong WJ, Zheng H, et al. $Ni_{12}P_5$ nanoparticles embedded into porous g-$C_3N_4$ nanosheets as a noble-metal-free hetero-structure photocatalyst for efficient $H_2$ production under visible light. J Mater Chem A 2017;5:16171–8.
[27] Yuan J, Wen J, Zhong Y, et al. Enhanced photocatalytic $H_2$ evolution over noble-metal-free NiS cocatalyst modified CdS nanorods/g-$C_3N_4$ heterojunctions. J Mater Chem A 2015;3:18244–55.
[28] Wu H, Chen Z, Zhang J, et al. Generalized synthesis of ultrathin cobalt-based nanosheets from metallophthalocyanine-modulated self-assemblies for complementary water electrolysis. Small 2018;14:1702896.
[29] Ye P, Liu X, Iocozzia J, et al. A highly stable non-noble metal $Ni_2P$ co-catalyst for increased $H_2$ generation by g-$C_3N_4$ under visible light irradiation. J Mater Chem A 2017;5:8493–8.
[30] Wang M, Liu Q, Xu N, et al. An amorphous $CoS_x$ modified $Mn_{0.5}Cd_{0.5}S$ solid solution with enhanced visible-light photocatalytic $H_2$-production activity. Catal Sci Technol 2018;8:4122–8.
[31] Yi SS, Yan JM, Wulan BR, et al. Noble-metal-free cobalt phosphide modified carbon nitride: an efficient photocatalyst for hydrogen generation. Appl Catal B Environ 2017;200:477–83.
[32] Yang Y, Zhang C, Huang D, et al. Boron nitride quantum dots decorated ultrathin porous g-$C_3N_4$: intensified exciton dissociation and charge transfer for promoting visible-light-driven molecular oxygen activation. Appl Catal B Environ 2019;245:87–99.
[33] Zhang S, Li J, Niu H, et al. Visible-light photocatalytic degradation of methylene blue using $SnO_2$/α-$Fe_2O_3$ hierarchical nanoheterostructures. ChemPlusChem 2013;78:192–9.
[34] Zhang S, Yang H, Gao H, et al. One-pot synthesis of CdS irregular nanospheres hybridized with oxygen-incorporated defect-rich $MoS_2$ ultrathin nanosheets for efficient photocatalytic hydrogen evolution. ACS Appl Mater Interfaces 2017;9:23635–46.
[35] Wen J, Xie J, Shen R, et al. Markedly enhanced visible-light photocatalytic $H_2$ generation over g-$C_3N_4$ nanosheets decorated by robust nickel phosphide ($Ni_{12}P_5$) cocatalysts. Dalton Trans 2017;46:1794–802.
[36] Zeng D, Xu W, Ong WJ, et al. Toward noble-metal-free visible-light-driven photocatalytic hydrogen evolution: monodisperse sub–15 nm $Ni_2P$ nanoparticles anchored on porous g-$C_3N_4$ nanosheets to engineer 0D-2D heterojunction interfaces. Appl Catal B Environ 2018;221:47–55.
[37] Yu H, Shi R, Zhao Y, et al. Alkali-assisted synthesis of nitrogen deficient graphitic carbon nitride with tunable band structures for efficient visible-light-driven hydrogen evolution. Adv Mater 2017;29:1605148.
[38] Yu Y, Yan W, Wang X, et al. Surface engineering for extremely enhanced charge separation and photocatalytic hydrogen evolution on g-$C_3N_4$. Adv Mater 2018;30:1705060.
[39] Qiu B, Zhu Q, Du M, et al. Efficient solar light harvesting CdS/$Co_9S_8$ hollow cubes for Z-scheme photocatalytic water splitting. Angew Chem Int Ed 2017;56:2684–8.
[40] Zhang X, Liu Y, Gao J, et al. Defect-rich (Co–$CoS_2$)$_x$@$Co_9S_8$ nanosheets derived from monomolecular precursor pyrolysis with excellent catalytic activity for hydrogen evolution reaction. J Mater Chem A 2018;6:7977–87.
[41] Wang JY, Ouyang T, Li N, et al. S, N co-doped carbon nanotube-encapsulated core-shelled $CoS_2$@Co nanoparticles: efficient and stable bifunctional catalysts for overall water splitting. Sci Bull 2018;63:1130–40.
[42] Chen Y, Li W, Jiang D, et al. Facile synthesis of bimodal macroporous g-$C_3N_4$/$SnO_2$ nanohybrids with enhanced photocatalytic activity. Sci Bull 2019;64:44–53.
[43] Luan S, Qu D, An L, et al. Enhancing photocatalytic performance by constructing ultrafine $TiO_2$ nanorods/g-$C_3N_4$ nanosheets heterojunction for water treatment. Sci Bull 2018;63:683–90.
[44] Zhao H, Ding X, Zhang B, et al. Enhanced photocatalytic hydrogen evolution along with byproducts suppressing over Z-scheme $Cd_xZn_{1-x}S$/Au/g-$C_3N_4$ photocatalysts under visible light. Sci Bull 2017;62:602–9.
[45] Xin Y, Huang Y, Lin K, et al. Self-template synthesis of double-layered porous nanotubes with spatially separated photoredox surfaces for efficient photocatalytic hydrogen production. Sci Bull 2018;63:601–8.
[46] Liu X, Qin H, Fan W. Enhanced visible-light photocatalytic activity of a g-$C_3N_4$/M-$LaVO_4$ heterojunction: band offset determination. Sci Bull 2016;61:645–55.
[47] Dong X, Cui W, Wang H, et al. Promoting ring-opening efficiency for suppressing toxic intermediates during photocatalytic toluene degradation via surface oxygen vacancies. Sci Bull 2019;64:669–78.
[48] Liu S, Zheng L, Yu P, et al. Novel composites of α-$Fe_2O_3$ tetrakaidecahedron and graphene oxide as an effective photoelectrode with enhanced photocurrent performances. Adv Funct Mater 2016;26:3331–9.
[49] Zheng L, Han S, Liu H, et al. Hierarchical $MoS_2$ nanosheet@$TiO_2$ nanotube array composites with enhanced photocatalytic and photocurrent performances. Small 2016;12:1527–36.

Hongcen Yang joined School of Physics and Technology, University of Jinan for his Master degree in 2016. His research focuses on photocatalytic $H_2$ production and photocatalytic degradation of organic pollutants.

Xijin Xu received his Ph.D. degree in Institute of Solid State Physics, Chinese Academy of Sciences in 2007. He conducted his postdoctoral research at Nanyang Technological University, Singapore in 2007 and then joined National Institute for Materials Science, Japan and Griffith University in Australia. Currently, he is a full professor in University of Jinan. His research interests include the synthesis and characterization of functional micro/nanostructures and their applications in environmental remediation and energy storage.